Engineering xxx (xxxx) xxx

Contents lists available at ScienceDirect

Engineering

journal homepage: www.elsevier.com/locate/eng

Research
Agricultural Sensors—Article

Design, Characterization, and Application of a Continuously Tunable Wavelength Spatial Frequency Domain Imaging System for Measuring the Optical Properties of Fruits

Yuan Gao [a,b,c], Zhizhong Sun [a,b,c,d], Xuan Luo [a,b,c], Dong Hu [e], Benhui Dai [f], Yingjie Zheng [a,b,c,g], Yibin Ying [a,b,c], Lijuan Xie [a,b,c,*]

[a] College of Biosystems Engineering and Food Science, Zhejiang University, Hangzhou 310058, China
[b] The National Key Laboratory of Agricultural Equipment Technology, Beijing 100083, China
[c] Key Laboratory of Intelligent Equipment and Robotics for Agriculture of Zhejiang Province, Science Technology Department of Zhejiang Province, Hangzhou 310058, China
[d] College of Chemistry and Materials Engineering, Zhejiang A&F University, Hangzhou 311300, China
[e] College of Optical, Mechanical and Electrical Engineering, Zhejiang A&F University, Hangzhou 311300, China
[f] CREATE Lab, École Polytechnique Fédérale de Lausanne (EPFL), Lausanne 1015, Switzerland
[g] Department of Computer Science, University College London (UCL), London WC1E 6BT, United Kingdom

ARTICLE INFO

Article history:
Received 18 May 2025
Revised 17 December 2025
Accepted 5 January 2026
Available online xxxx

Keywords:
Spatial frequency domain imaging
Optical properties
Tunable wavelength system
Noncontact optical imaging
Fruit quality inspection

ABSTRACT

Spatial frequency domain imaging (SFDI) has been widely applied in fruit quality inspection because of its noncontact and wide-field advantages. However, conventional multispectral SFDI systems remain constrained by low transmission efficiency, limited spectral range, and reliance on mechanical scanning. To overcome these limitations, we developed a continuously tunable wavelength SFDI system (450–1040 nm) that enables both continuous-spectrum and selectable-band imaging through patterned monochromatic illumination. The system adopts a modular design that integrates a monochromatic light generation module, a projection module, an imaging module, and a motorized imaging platform. This configuration allows flexible coupling and replacement of light sources and projection modules, enabling automated measurement of optical properties across different wavelength ranges according to application needs. With its high tunability, the system supports customized measurements at specific wavelengths via dedicated acquisition software, and it also provides the potential for spectral extension into longer infrared bands by simply upgrading the light source and infrared-sensitive projection module. Leveraging its wavelength tunability, we further demonstrated the system's capability for depth-resolved imaging by jointly regulating the spatial frequency and wavelength. The results showed that the system achieved an imaging depth of 3–4 mm. The optical property measurements of various fruits obtained using our system were in close agreement with the reference values provided by the integrating sphere (IS). The mean measurement error of the absorption coefficient (μ_a) was approximately 0.002 mm^{-1}, while that of the reduced scattering coefficient (μ_s') was approximately 0.02 mm^{-1}. In the application case of peach firmness prediction, the developed model achieved a coefficient of determination for prediction (R_p^2) of 0.786. These results demonstrate that our system is more accurate than existing multiwavelength SFDI devices. This improvement indicates that the extended spectral range of the proposed SFDI system provides richer tissue information, thereby highlighting its potential for fruit quality evaluation. More importantly, this work establishes a new paradigm for SFDI instrumentation by transitioning from fixed multispectral sensing to customizable, spectrally continuous imaging, thereby broadening its applicability in the nondestructive evaluation of agricultural products and potentially other biological tissues.

1. Introduction

Fruit quality plays a vital role in determining consumer acceptance and market value. It comprises two main components:

* Corresponding author.
E-mail address: ljxie@zju.edu.cn (L. Xie).

https://doi.org/10.1016/j.eng.2026.01.029

Please cite this article as: Y. Gao, Z. Sun, X. Luo et al., Design, Characterization, and Application of a Continuously Tunable Wavelength Spatial Frequency Domain Imaging System for Measuring the Optical Properties of Fruits, Engineering, https://doi.org/10.1016/j.eng.2026.01.029

internal quality, such as the soluble solids content (SSC), acidity, and phenolic compounds, and external quality, which is related to size, color, shape, and surface defects. Accurate assessments of both internal and external fruit quality are essential for reducing economic losses in the supply chain, maintaining market competitiveness, and ensuring profitability for producers [1]. With the aging and decline of the agricultural workforce, there is a growing need to utilize intelligent machines to replace human labor [2]. Optical imaging and spectroscopic techniques, as automated inspection methods, have been extensively employed for fruit quality evaluation, with the majority of these methods relying on direct analysis of the total detected light signals [3]. However, these techniques cannot separate the effects of tissue absorption and scattering, making them sensitive to external system configurations and hindering model transferability [4]. Optical properties, specifically the absorption coefficient (μ_a) and the reduced scattering coefficient (μ_s'), are intrinsic tissue parameters that provide a direct link to quality attributes, making them valuable for cross-study comparisons and standardization. Established methodologies for measuring these parameters in fruits include integrating sphere (IS), time-resolved (TR), and spatially resolved (SR) methods [5]. Nevertheless, these conventional techniques are restricted to single-point measurements, rendering them unsuitable for wide-field optical characterization of heterogeneous fruit tissues.

As an emerging optical imaging technology, spatial frequency domain imaging (SFDI) enables noncontact, wide-field characterization of the optical properties of biological tissues [6]. Its initial applications in agriculture were demonstrated through apple tissue analysis, where SFDI successfully differentiated healthy from damaged tissues through optical property mapping [7]. Subsequent advancements by the United States Department of Agriculture Agricultural Research Service (USDA/ARS) in Michigan (USA) and the Intelligent Bioindustrial Equipment Innovation Team (IBE) at Zhejiang University (Hangzhou, China) extended SFDI applications to multidimensional fruit quality assessment, including multilayer optical parameter separation and surface bruise detection [8–12]. The conceptual prototype of SFDI was first proposed by Dögnitz and Wagnières in 1998 [13]. Its major components included a xenon arc lamp for illumination, a charge-coupled device (CCD) camera that served as the imaging sensor, and a projection module consisting of a patterned glass plate. Early implementations utilized broadband composite images without spectral discrimination [14,15], significantly limiting wavelength-specific optical characterization. This limitation is particularly problematic in fruit tissue analysis, where μ_a exhibits wavelength-dependent correlations with internal constituents such as anthocyanins, chlorophyll, and water [16]. Targeted spectral characterization facilitates not only optimal wavelength selection for enhanced imaging contrast but also quantitative prediction models for biochemical composition [17,18]. A critical drawback of early SFDI systems was their limited spectral coverage, often restricted to fewer than three discrete wavelengths [19].

Subsequent research has increasingly focused on spectral expansion strategies, yet the three fundamental bottlenecks of spectral span, spectral agility and system throughput remain unresolved. The spectral resolution of such systems is determined mainly by the coupling of the illumination sources, wavelength selectors, and imaging sensors.

In terms of illumination, the most common sources are light-emitting diodes (LEDs), lasers, and quartz tungsten halogen (QTH) lamps. By combining multiple LEDs at different wavelengths, multispectral SFDI can be achieved. However, the use of multiple LEDs increases system complexity, and the inherent spectral shifts in LEDs necessitate pre-experimental wavelength calibration [20].

Alternatively, broadband light sources such as xenon or halogen lamps combined with wavelength selection elements, such as bandpass filters or liquid crystal tunable filters (LCTFs), can also be used to achieve multispectral SFDI [7,19]. While bandpass filters are suitable for a limited number of wavelengths, increasing the number of spectral channels complicates the optical design. Moreover, LCTFs typically exhibit transmission efficiencies less than 50%, requiring longer exposure times and thus reducing system throughput. Other custom devices have also been explored for wavelength selection in SFDI systems. Torabzadeh et al. [21] employed a laser-based supercontinuum light source in conjunction with bandpass filtering via a folded-prism Martinez compressor, along with platform scanning to achieve imaging across the 580–950 nm range. However, the mechanical scanning components introduce system complexity. Subsequently, custom-built digital micromirror devices (DMDs) were implemented to enable rapid wavelength switching [22], yielding average measurement errors of 23% for μ_a and 6% for μ_s'. However, the DMD's restricted active area limited the usable spectral bandwidth to approximately 140 nm.

For imaging sensors, cameras are typically used to collect reflectance from the sample surface. By combining broadband sources with hyperspectral cameras, hyperspectral SFDI can be realized. One early implementation used an external push–broom hyperspectral imager to acquire 120 wavelengths per pixel over the 400–900 nm range, demonstrating its utility in pharmacokinetic studies [23]. More recently, researchers have integrated a built–in push–broom hyperspectral camera for SFDI, successfully measuring the optical properties of milk and predicting its fat and protein content [24]. Nevertheless, reliance on a motorized scanning stage continues to add mechanical complexity, and the inherently push–broom imaging mode prevents real-time imaging capabilities. In addition to push-broom systems, a computed tomography imaging spectrometer (CTIS) has been employed for hyperspectral SFDI. By diffracting multiple spectral images onto a single CCD chip to acquire the spectrum of each pixel, CTIS eliminates the need for spatial scanning; however, it can provide only limited spatial resolution (156×116 pixels) [25].

In summary, although recent developments in SFDI systems have increasingly emphasized spectral expansion, several challenges remain. Using combinations of multiple wavelength sources leads to increased system complexity, while broadband sources combined with wavelength selection elements still suffer from low transmission efficiency, limited spectral range, and mechanical scanning requirements. Hyperspectral cameras based on line scanning can eliminate the need for wavelength selection elements, but this approach results in a limited field of view (FOV) per acquisition and still requires mechanical scanning, further complicating system design. To overcome these limitations, we present a grating-based, continuously tunable SFDI system that delivers 450–1040 nm coverage in a single, static optical path. A 300 W xenon arc lamp is filtered by a monochromator (full width at half maximum (FWHM) less than 35 nm for wavelengths below 940 nm) and delivered to the sample through a 9.5 mm fiber bundle and a DMD projector; no mechanical scanning is needed. The modular control framework synchronizes grating rotation, DMD pattern upload, and camera capture. Finally, the snap-in fiber and camera module can accommodate alternative gratings or light sources without requiring realignment of the projection and imaging axes, thereby providing an upgraded path extending to 2500 nm for future agri-food applications.

2. Materials and methods

2.1. Construction of the continuously tunable wavelength SFDI sensing system

The continuously tunable wavelength SFDI sensing system developed in this study is illustrated in Fig. 1 and primarily

consists of four components: a monochromatic light generation module, a projection module, an imaging module, and a motorized imaging platform.

The monochromatic light generation module employs a 300 W xenon lamp (CME-TLSX300F; Microenerg, China) to provide stable broadband illumination over a spectral range of 200–1800 nm. Wavelength selection is achieved using a monochromator (CME-Mo151; Microenerg), equipped with two interchangeable gratings (CME-G1200-300 and CME-G600-1000; Microenerg), enabling center wavelength tuning across the 300–2000 nm range with 0.1 nm resolution. A focusing assembly is positioned between the light source and the monochromator to ensure efficient optical coupling. The projection module incorporates a projection assembly (V-650 L, ViALUX; Chemnitz, Germany), which includes a control unit and a DMD chip. A 9.5 mm core diameter multicore optical fiber (BXS3748M, Dolan-Jenner; Boxborough, USA) transmits light from the monochromator to the projection unit. A custom-designed three-dimensional (3D)-printed adapter ensures tight coupling between the fiber and the projection module's optical input, minimizing light leakage. After modulation by the DMD, the structured light is projected onto the sample through a projection lens (RAY-65; Dlinnovation, USA). The imaging module consists of a visible-light-enhanced near-infrared (NIR) camera (Bobcat 640, Xenics; France) that operates in the 450–1700 nm range, paired with a lens (M2514-VSW; DAHENG IMAGING, China). The imaging platform includes a motorized vertical spindle supporting the projection and imaging modules, a rotation stage for adjusting the angle between the projection and imaging axes, and a motorized lifting platform for sample placement. The imaging module is aligned perpendicular to the sample stage. On the basis of previous studies [16,26,27], the angle between the projector and the camera was set to 12° to minimize distortion of the projected patterns. The horizontal distance between the projection and imaging optical centers was set to 6 cm, as determined by preliminary tests. In practice, this distance should be minimized to reduce projection distortion and maximize the field-of-view overlap. The final imaging height was fixed at 23 cm, optimized to accommodate the size range of common fruits. For fruits of different sizes, the height was adjusted by regulating the motorized lifting platform to ensure a consistent imaging distance, thereby reducing systemic deviations caused by adjustments in projection and camera positioning. The entire SFDI system was placed on an optical platform to ensure structural stability, and the projection module, imaging module, and imaging platform were enclosed within a dark box to prevent interference from ambient light.

2.2. Design of the modular control platform

In the developed SFDI system, the imaging process primarily involves wavelength selection, structured pattern projection, and image acquisition. However, each hardware component is controlled by independent software provided by the respective manufacturers, resulting in considerable complexity when imaging modes that require sequential scanning across both wavelength and spatial frequency (f_x) domains are implemented. To address this challenge and achieve full system automation, we developed a modular control platform for the continuously tunable broadband SFDI system, built on the Sunny.UI framework. The user interface of the software is illustrated in Fig. S1 in Appendix A. The main interface integrates a task management panel, a real-time logging module, and comprehensive device control components. It dynamically displays key experimental parameters, including grating selection, exposure time, operational delay, current projection pattern name, and overall system status. A synchronized logging system, with timestamped entries, records feedback from the three core devices-monochromator, projector, and camera-enabling real-time monitoring of device operations and error reporting. The control software reads an editable input file that specifies the target wavelengths, associated gratings, spatial frequencies, and corresponding camera exposure times. This enables high flexibility for acquiring customized wavelength-dependent datasets in an automated manner.

2.3. Image processing and analysis

The measurement of optical properties in biological tissues using SFDI technology typically involves three main steps: image acquisition, demodulation, and optical properties estimation. In

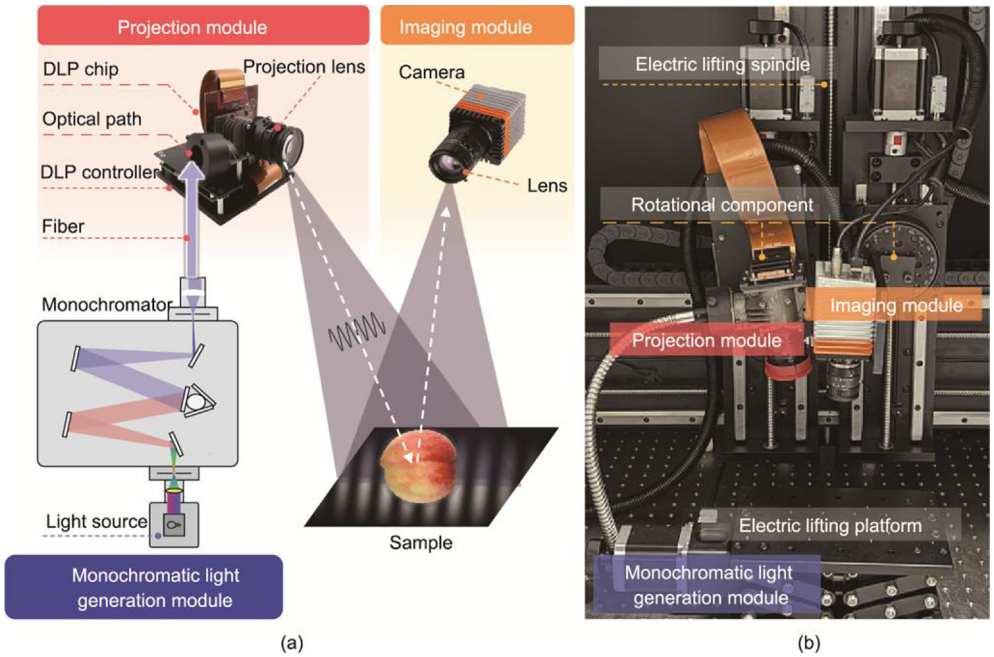

Fig. 1. Schematic diagram of (a) the constructed SFDI system and (b) the experimental setup. DLP: digital light processing.

the first step, a series of images are captured using combinations of multiple f_x and phase shifts across different wavelengths. In this study, phase shifts of 0°, 120°, and 240° were selected for the spatial phase α. To investigate the impact of f_x on light penetration depth, a wider range of f_x, including 0, 0.01, 0.03, 0.05, 0.07, 0.10, 0.15, 0.20, 0.25, and 0.30 mm^{-1}, was used. For phantom and fruit sample measurements, considering the trade-off between sampling time and light penetration depth, a zero f_x (0 mm^{-1}) and a high f_x (0.2 mm^{-1}) were selected. Diffuse reflectance values corresponding to each frequency were extracted using the conventional three-phase demodulation algorithm. The optical properties of the sample can subsequently be derived from the diffuse reflectance values at two or more frequencies, combined with least squares curve fitting [28]. The detailed data processing procedures are described in our previous work [29].

2.4. System characterization

2.4.1. FOV and spatial resolution

The FOV is a commonly used metric to characterize the visible area covered by a machine vision system. In contrast to conventional imaging systems, the FOV of an SFDI system is influenced not only by the camera optics but also by the effective illumination area provided by the projection module. Since the imaging height of the system was fixed at 23 cm, the FOV was represented as the actual two-dimensional (2D) area at this distance. To accommodate the imaging of fruits of varying sizes, characterization of the system's FOV is essential. After the focal length of the imaging lens was determined, a custom-designed test target consisting of nine concentric circles with radii ranging from 1 to 9 cm was fabricated. During testing, the target was placed atop a diffuse white board (YMBXC3; Jinshuimu Optoelectronics, China) to ensure a flat and uniform background.

Spatial resolution, traditionally defined as the minimum separation distance at which two objects can still be distinguished, is another critical metric for assessing the performance of machine vision systems [30]. In the context of SFDI, high spatial resolution enables more accurate representation of fine structural features. In this study, spatial resolution was evaluated using a USAF 1951 resolution target (GCG-020601; Daheng Optics, China), following the methodology described in previous literature [31]. The target, measuring 50.8 mm in overall dimensions and approximately 15 mm × 14 mm in the central patterned area, includes 42 elements spanning from Group 0 to Group (7). These elements cover spatial frequencies from 1 line pair per millimeter (lp·mm^{-1}) (Group 0, Element 1) to 228 lp·mm^{-1} (Group (7), Element 6). Since we used the positive version of the USAF 1951 target (a chromium pattern on a transparent background), we placed it in reverse orientation to eliminate shadow artifacts while maintaining sharp imaging of the target. The system's resolving capability was quantified by calculating the peak-to-valley ratio (PVR) of the image intensity profiles for different elements. A group/element was considered resolvable if the corresponding PVR exceeded $\sqrt{2}$. The spatial resolution of the SFDI system, expressed in lp·mm^{-1}, was then determined on the basis of the highest resolvable element, as identified using the USAF 1951 resolution target lookup table.

2.4.2. Characterization of the system output wavelength

To obtain sample data under illumination at a specific wavelength, a monochromator is required for wavelength selection. Previous research has utilized the characteristic emission spectrum of a mercury–argon lamp for spectral calibration [32]. In this study, to assess the wavelength output accuracy of the constructed SFDI system under continuous wavelength variation, a miniature spectrometer (QE65 Pro; Ocean Optics, USA) was used to measure the spectral output of the projection module. During the evaluation, the spectrometer was positioned on the imaging platform within the dark box of the SFDI system, with the fiber optic input port aligned directly toward the projection lens. The system was programmed to scan wavelengths from 450 to 1040 nm in 10 nm increments. At each wavelength step, three spectral measurements were collected and averaged to improve reliability. The spectrometer's exposure time was preset on the basis of the maximum light intensity observed during preliminary tests to prevent saturation and was held constant throughout the experiment. Each spectral output from the monochromator was fitted using a Gaussian function with a constant baseline, calculated using Eq. (1):

$$y(x) = Ae^{\left(-\frac{(x-\mu)^2}{2\sigma^2}\right)} + y_0 \tag{1}$$

where x is the wavelength, $y(x)$ is the measured spectral intensity, μ is the fitted center wavelength, A is the peak amplitude above the baseline, σ is the standard deviation of the Gaussian distribution, and y_0 is the baseline offset. The FWHM of the Gaussian peak was derived from σ using Eq. (2):

$$\mathrm{FWHM} = 2\sqrt{2\ln 2}\sigma \tag{2}$$

2.5. System calibration

2.5.1. Uniformity correction

Owing to the difficulty in achieving perfect uniformity in the optical path design of the projection components, the light exiting the monochromator tends to be more concentrated in the central region than in the peripheral regions after passing through a series of optical elements and reaching the projection lens. This results in higher brightness in the center of the acquired images. To achieve more accurate measurements of sample surface reflectance and ensure accurate fitting results for optical properties parameters, Eq. (3) was used to correct the uniformity of the acquired images:

$$R_{\mathrm{corrected}} = \frac{I - I_{\mathrm{dark}}}{I_{\mathrm{white}} - I_{\mathrm{dark}}} \tag{3}$$

where $\boldsymbol{I}$ is the raw image intensity of the sample, I_{white} is the image intensity of the diffuse white board under the projected pattern, and I_{dark} is the dark field image intensity acquired with the light source turned off. The diffuse white board used in practice, along with the acquired diffuse white board and sample SFDI images, are shown in Figs. S2(a)–(c) in Appendix A (the solid optical phantoms used for subsequent linearity correction and their measurement results are sequentially presented in Figs. S2(d)–(k) in Appendix A). Notably, the recorded light intensity is also affected by the optical path length; therefore, during image acquisition, the height of the diffuse white board and the top surface of the sample should be kept consistent.

To verify the uniformity of the corrected images, we adopted the uniformity of the structured light metric from related research [19], which is calculated as follows:

$$\delta = \frac{V_{\max} - V_{\min}}{V_{\min}} \tag{4}$$

where δ represents the degree of image uniformity, and $V_{\min}$ and $V_{\max}$ represent the minimum and maximum peak values, respectively, of the average intensity of the sinusoidal pattern in the image.

2.5.2. Construction of the optical properties reference system and linearity correction of the SFDI system

Most diffuse optics techniques, including SFDI, rely on calibration measurements to determine the instrument response function (IRF). This function compensates for inherent system

characteristics-such as the relative angles of the projector and camera-thereby enabling accurate quantification of optical properties [20]. Establishing a linear relationship between measured and true optical properties across various wavelengths helps mitigate nonlinear artifacts and improves measurement accuracy [3,33]. Optical phantoms are typically used for this linearity correction. Their reference values are typically derived using thin-sheet phantoms measured in an IS system, combined with the inverse adding-doubling (IAD) method, which is widely regarded as the gold standard for optical property determination [34]. In this study, an IS system was constructed to obtain reference optical properties. A 20 W direct current (DC)-regulated fiber optic light source (HL-2000-FHSA; Ocean Optics) provided collimated illumination via a fiber-coupled collimator (F240SMA-B; Thorlabs, USA). The IS used had a diameter of 83.8 mm and a Spectralon coating (4P-GPS-033-SL; Labsphere, USA). The equatorial port served as both the entrance and exit for light, while the detection port, located at the north pole, was connected to a spectrometer (QE65Pro, Ocean Optics) via optical fiber. To avoid direct entry of collimation components into the IS and interference with its diffuse reflectance, the collimator was positioned outside the sphere. During all the measurements, the light source was placed at a distance equal to one IS diameter from the sphere to ensure a consistent spot size. Inputs for the IAD algorithm are detailed in Table 1, and further experimental procedures are described in [35]. The final optical properties were calculated using the IAD algorithm [36]. For all the IS measurements, the raw spectra were manually acquired three times and averaged, with each spectrum internally averaged five times by the acquisition software.

To evaluate the measurement accuracy of the IS system, we used liquid optical phantoms to characterize the system's precision. To assess the accuracy of μ_a, we used pure water and India ink (Royal Talens, Netherlands). To evaluate μ_s', we selected Intralipid-20% (Fat Emulsion Injection; FRESENIUS KABI SSPC, China). The volume concentrations of the India ink solutions ranged from 0.01% to 0.10% (in 0.01% increments), while the volume concentrations of the fat emulsion solutions were 1%, 3%, and 5%. The reference μ_a for the India ink solutions was measured using the collimated transmission method. The optical properties of pure water and Intralipid-20% solutions were referenced from the relevant literature [37–39].

The phantoms used for linearity correction of SFDI need to satisfy the semi-infinite and thin-sheet characteristics. Considering the potential instability of liquid phantoms during prolonged measurements in this study, we chose to prepare solid optical phantoms using polydimethylsiloxane (PDMS), following the specific preparation steps outlined in published research [40,41]. The μ_a of the solid optical phantoms was also adjusted by adding India ink, while titanium dioxide (TiO_2) (titanium oxide, 40 nm; Macklin Biochemical, China) was used to adjust the μ_s'. The volume concentrations of India ink and TiO_2 in the five prepared phantoms were 0.01%, 0.03%, 0.05%, 0.10%, and 0.15% and 0.05%, 0.07%, 0.10%, 0.15%, and 0.20%, respectively. The dimensions of the bulk phantoms used for the SFDI measurements were 50 mm × 50 mm × 50 mm, and the dimensions of the thin-sheet phantoms used for the IS measurements were 50 mm × 50 mm × 2 mm. The prepared thin-sheet phantoms and bulk phantoms are shown in Figs. S2(d) and (h) in Appendix A, respectively. Their optical properties were measured using the IS (Fig. S2(e) in Appendix A) and the SFDI system (Fig. S2(i) in Appendix A), with the results presented in Figs. S2(f), (g), (j), and (k) in Appendix A. The measurement procedures for total reflectance and transmittance of the IS system are illustrated in Figs. S3(a) and (b) in Appendix A, respectively. By performing linear regression on the optical properties of five phantoms at each wavelength, wavelength-specific correction equations were established for subsequent SFDI measurements.

Table 1
The input parameters of the IAD program.

IAD input parameters	Samples	Values or conditions
Basic parameters		
Beam diameter	—	11.0 mm
Sample thickness	Water	5.0 mm
	Indian ink, Intralipid	3.0 mm
	Fruit samples	Measured value
Sample index of refraction	—	1.34
Top slide thickness	—	Measured value
Bottom slide thickness	—	Measured value
Top slide index of refraction	—	1.53
Bottom slide index of refraction	—	1.53
Anisotropy factor	Water	0
	Indian ink, Intralipid, and fruit samples	0.7
Number of integrating spheres	—	1
Parameters of reflection sphere		
Diameter	—	83.8 mm
Sample port diameter	—	25.4 mm
Entrance port diameter	—	25.4 mm
Detector port diameter	—	3.0 mm
Wall reflectance	—	98.0%
Standard reflectance	—	98.0%
Detector reflectance	—	0
Parameters of transmission sphere		
Diameter	—	83.8 mm
Sample port diameter	—	25.4 mm
Entrance port diameter	—	0 mm
Detector port diameter	—	3.0 mm
Wall reflectance	—	98.0%
Standard reflectance	—	100.0%
Detector reflectance	—	0

2.6. Performance evaluation of the system light penetration depth

A distinguishing advantage of SFDI over traditional planar illumination-based techniques is its capacity for depth-resolved imaging. In previous studies, the imaging depth of SFDI systems was evaluated by overlaying standard white printing paper atop USAF 1951 resolution targets or Snellen eye charts containing black characters of varying sizes [12]. White printing papers may vary in color across manufacturers and even between batches. In addition, the gaps between paper layers differ from the homogeneous structure of biological tissues. Therefore, we constructed a liquid phantom pool to evaluate the penetration capability of the SFDI system. Similar phantom pools have been created by drilling holes in nylon plates, but the unknown optical properties of the nylon plates make it difficult to quantitatively assess the relationship between optical properties and penetration depth [27]. The phantom pool model designed in this study is shown in Fig. S4 in Appendix A. The external structure was printed using a 3D printer (Bambu Lab X1; Bambu Lab, China) with white polylactic acid (PLA) as the material. The background phantom depth was 50 mm, and the subject phantom was placed inside capillaries (DK060708; Longreen, China) with diameters of 4 and 2 mm, positioned at multiple heights ranging from 1–4 mm below the liquid surface. Similar to the study by Zhao et al. [42], we chose to configure the subject phantom as a highly absorbing solution. Specifically, we filled the capillaries with 0.1% of India ink, while the background

phantom was composed of a mixture of 0.01% India ink and 2% Intralipid-20% solution. The results of our preliminary experiments revealed that the prepared background phantom closely resembled the average optical properties of common fruit peels [5,43].

2.7. Measurement of the optical properties of fruits

To further evaluate the accuracy of the constructed SFDI system in measuring the optical properties of real fruit samples, we compared and analyzed the optical properties measured by the SFDI system with those measured by the IS. The selected fruit samples were Spring Snow peaches, Fuji apples, and Crown pears, which were all purchased from a local supermarket. The fruit sample ultimately used to showcase optical properties under a wide FOV was a locally grown (Hangzhou) red peach, chosen to better highlight differences in pigment absorption peaks. Because related research has shown that temperature can affect the molecular vibrations of fruit samples, thereby nonlinearly affecting their spectral properties [4,44], these samples were placed in a laboratory environment (temperature: 26 °C; humidity: 50%) for six hours prior to the experiment to avoid the influence of temperature changes during the measurement process. To compare the optical properties measured by the SFDI system with the results of the IS measurements, we approximated the small region of fruit tissue in the radial depth as a homogeneous object. First, a 3 to 4 cm thick portion near the surface of the fruit was peeled away, exposing a flat surface for SFDI, where the height of the fruit was controlled to 5 cm. After the SFDI system measurement was completed, a thin slice approximately 3 mm thick was further peeled from the surface for IS measurement.

2.8. Firmness prediction of peaches

In this study, 120 peaches (*Prunus persica* cv. 'Wuyuehong') harvested from Fuyang, Zhejiang Province, were used. For SFDI measurements, the outer surface of each peach was trimmed by approximately 8 mm along the suture line to obtain a flat acquisition surface. Prior to imaging, the opposite side of the fruit was leveled with a precision slicing machine (M20; Graef, Germany) to standardize the total height to 50 mm, ensuring consistent imaging conditions. Excess surface juice was gently absorbed with lens-cleaning paper to avoid interference from the microdroplets. After imaging, fruit firmness was measured using a GY-4 fruit hardness tester equipped with a cylindrical 11 mm diameter probe. The probe was manually pressed into the peach flesh until it reached the marked depth line (11 mm). The firmness value was recorded as the maximum force during penetration. For each peach, three measurement points were evenly distributed on the trimmed surface, and the mean value was used as the representative firmness.

Partial least squares regression (PLSR), a multivariate statistical method widely applied in chemometrics to model quantitative relationships between predictor and response variables [45], has been successfully employed in numerous studies on NIR modeling. In this work, PLSR was used to establish a predictive model of peach flesh firmness. Prior to modeling, the dataset was randomly divided into a calibration set (70%) and a prediction set (30%). To compare the influence of different optical inputs, models were developed using μ_a, μ_s', their product $\mu_a \times \mu_s'$, and the effective attenuation coefficient μ_{eff}. The μ_{eff} can be calculated as:

$$\mu_{eff} = \sqrt{3\mu_a(\mu_a + \mu_s')} \tag{5}$$

Model performance for peach firmness prediction was evaluated using the coefficient of determination for calibration (R_c^2) and prediction (R_p^2), as well as the root mean square error of calibration (RMSEC) and prediction (RMSEP). These parameters were calculated as follows:

$$R^2 = 1 - \frac{\sum_{i=1}^{n}(y_i - \hat{y}_i)^2}{\sum_{i=1}^{n}\left(y_i - \bar{y}\right)^2} \tag{6}$$

$$\mathrm{RMSE} = \sqrt{\frac{1}{n}\sum_{i=1}^{n}(y_i - \hat{y}_i)^2} \tag{7}$$

where y_i is the reference firmness value of the ith sample, $\hat{y}_i$ is the calibrated or predicted firmness value of the ith sample, $\bar{y}$ is the mean of the reference firmness value, and n is the number of samples.

3. Results and discussion

3.1. System characterization

3.1.1. FOV and spatial resolution

The FOV measurement results of the constructed SFDI system are shown in Fig. 2(a), with an approximate area of 9 cm × 11 cm. The diameter of medium-sized fruits currently available on the market is generally approximately 6–8 cm, such as oranges, apples, pears, and peaches, indicating that the system's FOV can meet the imaging requirements for small to medium-sized fruits. Fig. 2(b) shows the imaging results of the constructed system on the USAF 1951 target. The black artifacts between the stripes are due to the fact that the test target is made of glass, causing the surface pattern to form shadows at the bottom of the target. Fig. 2(c) shows the vertical intensity profile for Group (1), Elements 1–6. For the line pairs in Group (1), the PVRs from Element 0 to Element 6 were 2.14, 2.03, 1.81, 1.75, 1.47, and 1.35, respectively. We found that the PVR of Element 5 is greater than $\sqrt{2}$, while the PVR of Element 6 is less than $\sqrt{2}$. By consulting the standard table, we confirmed that the spatial resolution of this SFDI system is 3.17 lp·mm^{-1}. Considering that the vertical FOV of the system measured in this spatial resolution test was 110 mm and that the camera has 512 vertical lines, the highest spatial resolution of the image is 215 μm. In our application, the measured spatial resolution of 215 μm is sufficient to detect the surface texture of fruits.

3.1.2. Characterization and calibration of the system output wavelength

Fig. 3 presents the spectral measurements obtained from the spectrometer when the SFDI system was tuned to preset wavelengths. Fig. 3(a) shows the output light at different wavelengths after passing through the monochromator grating. As illustrated in Figs. 3(b)–(e), the system demonstrated stable spectral output within the 450–1040 nm range. By integrating a six-position filter wheel after the monochromator, the influence of the grating side peaks was effectively suppressed, and the output wavelength maintained a single-peak profile. The system exhibited relatively narrow FWHM values below 900 nm, with an average FWHM of less than 30 nm. However, at specific wavelengths beyond 940 nm, the FWHM broadened significantly.

To further clarify the difference between the measured and preset wavelengths, Fig. S5(a) in Appendix A displays the measured peak positions at selected preset wavelengths of 500, 650, 800, and 1000 nm. The absolute errors between the measured and preset peaks were 0.73, 0.76, 0.32, and 10.83 nm, respectively. Here, the maximum intensity position was chosen as the peak value. Fig. S5(b) in Appendix A compares the preset and measured peak positions across the 450–1040 nm range. The results indicate that in the 450–980 nm range, the measured peak positions closely matched the preset values. Beyond 980 nm, however, the deviation increased, which may be attributed to the low transmittance of the

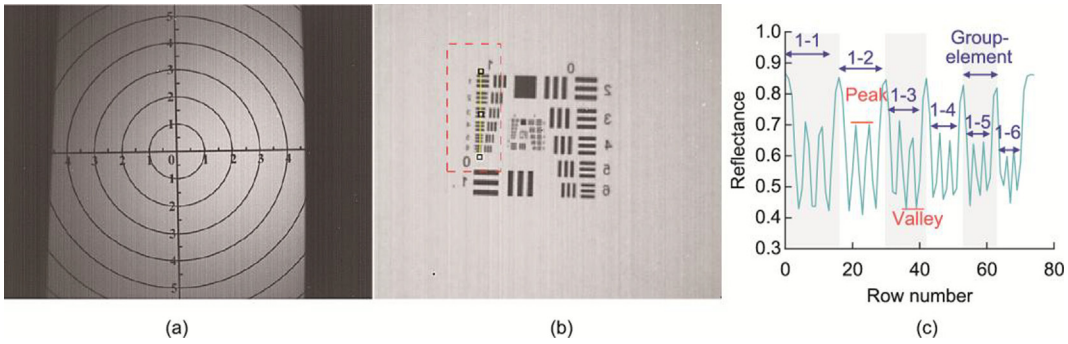

Fig. 2. SFDI system imaging characterization: (a) FOV measurement, (b) USAF 1951 resolution test, and (c) vertical intensity profile of Group (1), Elements 1–6.

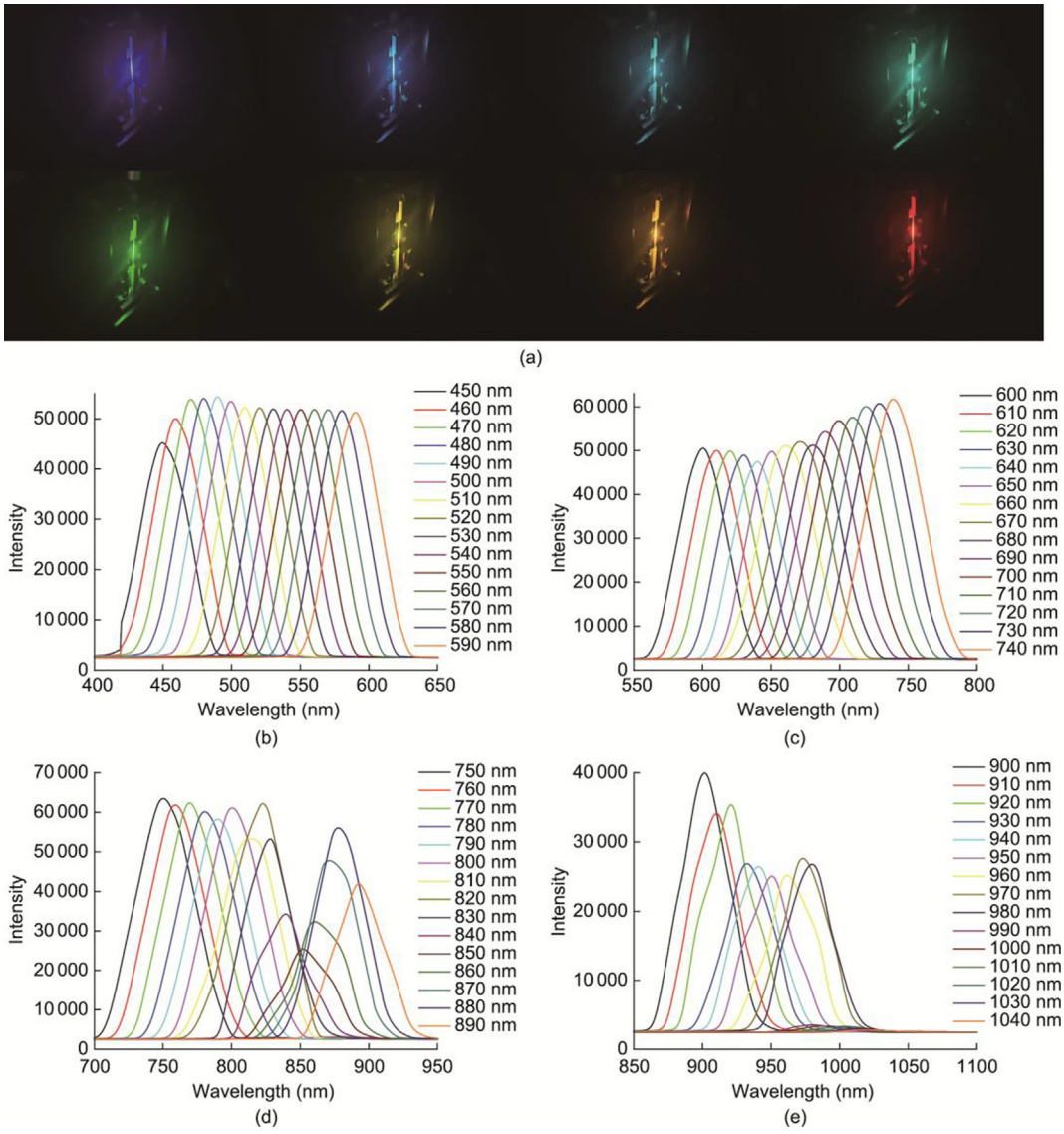

Fig. 3. Spectrometer measurement results of the SFDI system at specified wavelengths: (a) schematic illustration of the monochromator grating output at various wavelengths, (b) 450–590 nm, (c) 600–740 nm, (d) 750–890 nm, and (e) 900–1040 nm.

projection module in the infrared region. Nevertheless, since fruit quality inspection relies primarily on wavelengths below 980 nm (i.e., before the water absorption peak in the visible to NIR region), the system meets the requirements of this application. Across the entire tuning range, the mean deviation of the measured peaks was –0.929 nm, with a standard deviation of 4.312 nm, confirming the stability of the wavelength tuning. A linear relationship was established between the preset and measured peak positions, with a R^2 of 0.9995, demonstrating excellent wavelength tuning linearity.

3.2. System calibration

3.2.1. Uniformity correction

Fig. 4 shows the effect of the uniformity correction on the diffuse reflector image intensity. The first and second rows of the figure show white board images before and after uniformity correction, respectively. The first two columns display the white board images at a f_x of 0 mm^{-1}. The intensity map clearly shows that the light intensity in the central region of the image is greater than that in the peripheral regions before correction. This is because the projection lens directly illuminates the center of the white board and the hardware setup, causing a more concentrated central light source. After correction, the image intensity is more uniform across the entire 2D plane, and the coefficient of variation of the image intensity across the entire plane decreases from 46.31% before correction to 8.78%, significantly improving image uniformity. The intensity change curves of the white board images at a f_x of 0.2 mm^{-1}, shown in the fourth column, also reveal that the central intensity of the image is higher, and this situation leads to distortion of the curves that should exhibit a sinusoidal pattern. The contrast of the black and white stripes is significantly increased after correction, and the pattern more closely resembles a sinusoidal variation. The coefficient of variation of the peaks decreases from 9.04% before correction to 0.72%, and the coefficient of variation of the valleys decreases from 3.98% to 1.70% after correction. The results indicate that uniformity correction can significantly improve image uniformity and markedly reduce distortion in the captured projected images.

3.2.2. IS system validation

To verify the measurement stability of the IS system, the coefficients of variation (CV) for three types of samples across three repeated measurements are presented in Figs. 5(a)–(c). During these measurements, the cuvettes containing the liquid samples were placed in three different positions. Even under these conditions, the μ_a of the 0.01%–0.10% ink solutions and the μ_s' of the 1%–5% Intralipid-20% solutions both maintained low CV values. The CV for the μ_a of pure water is larger before 800 nm because the μ_a of water in this wavelength range, as shown in Fig. 5(d), is between 10^{-6} and 10^{-4}, and a lower μ_a leads to greater fluctuations in the measurement error. For the Intralipid-20% solution used for μ_s' validation, the measured CV increases with increasing concentration, with the average CV increasing from 0.19% to 0.62%. The tested ink samples at different concentrations maintained low CVs across multiple measurements. The sample with the highest CV was the 0.01% ink, with a value of 0.71%. The overall average CV across all wavelengths decreased with increasing ink concentration, with the lowest CV being 0.17%. These findings indicate that the liquid phantoms we used are highly uniform and that the test results of the constructed IS system are repeatable.

Furthermore, a comparison between the measured optical properties of water, ink, and Intralipid-20% solution and their reference values is shown in Figs. 5 (d)–(f). The results show that the μ_a of pure water is in good agreement with the standard values given in the relevant literature within the 400–1100 nm range. To avoid the disturbance of a smaller μ_a at shorter wavelengths, we evaluated the average relative error of μ_a in the 800–1100 nm range, which was within 7%. For the μ_a of ink, we found that the average relative error range of the μ_a measurements for different concentrations was 1.24%–5.06% within the 450–1040 nm range, and in the samples we constructed, the higher the concentration of ink was, the smaller the measurement error. With respect to the Intralipid-20% solution, μ_s' increases with increasing concentration, while the difference from the standard value decreases. The average relative error of μ_s' with different concentrations was 7.53%. The above results indicate that the IS system we constructed has high measurement accuracy and can be used as a reference for standard measurements in the SFDI system.

3.2.3. Linearity correction

Fig. S6 presents a diagram of the linearity correction results for the SFDI system. As shown in Fig. S6(a) in Appendix A, both μ_a and μ_s' exhibit good linearity at several randomly selected wavelengths. The linearity of μ_s' is particularly good, with R^2 all greater than 0.99. However, the R^2 for μ_a is somewhat lower at certain

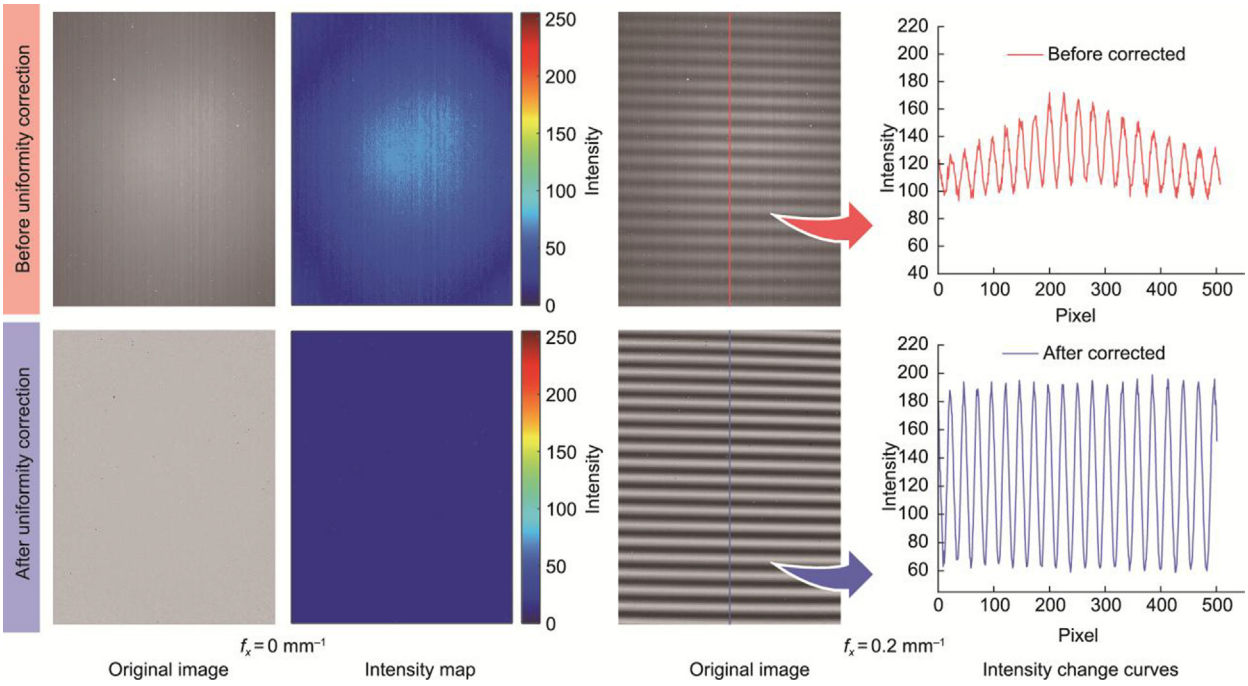

Fig. 4. Effect of uniformity correction on diffuse reflector image intensity.

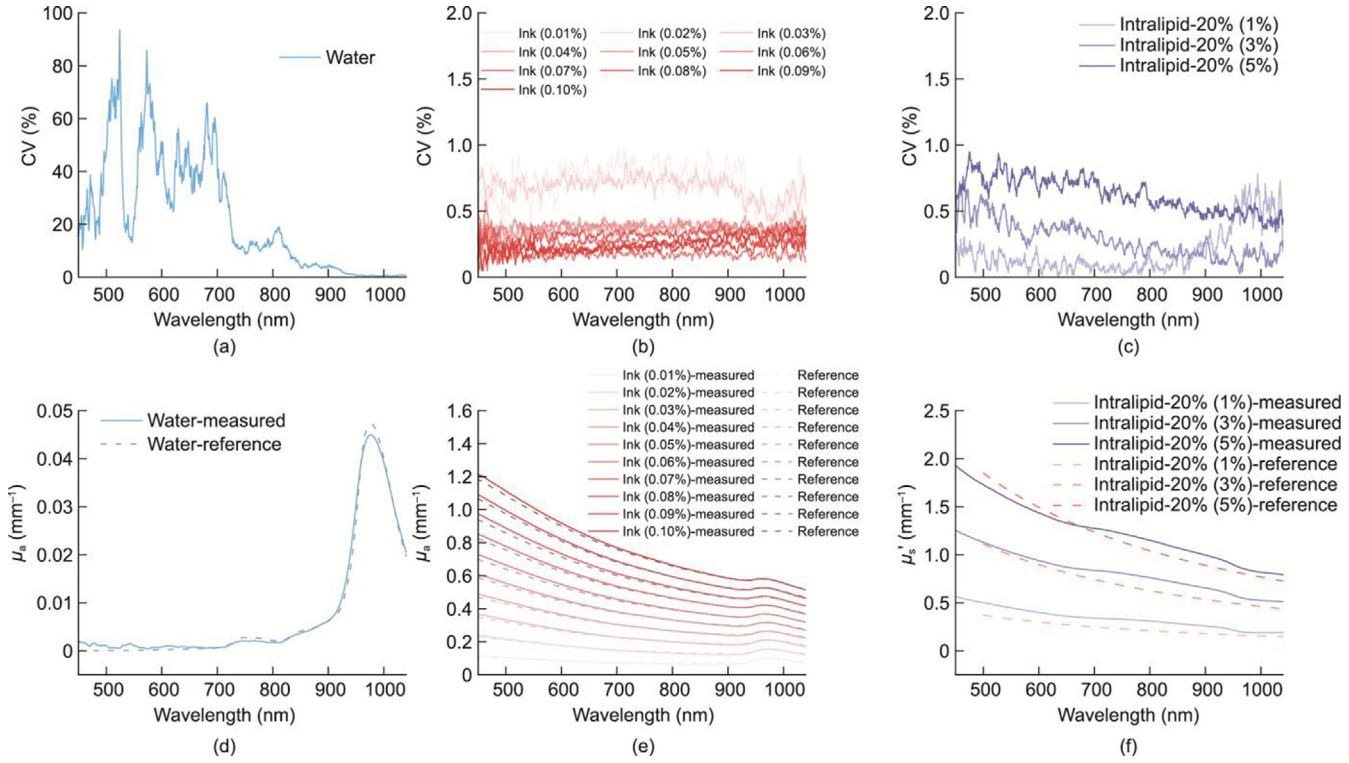

Fig. 5. CV measurement results of (a) water, (b) ink, and (c) Intralipid-20% solution; comparison between the measured optical properties of (d) water, (e) ink, and (f) Intralipid-20% solution and their reference values.

wavelengths, such as 450 nm, potentially because of the weaker system response at the edges of the system's wavelength range. On the basis of the results in Fig. S6(b) in Appendix A, we analyzed the system's optical properties fitting results across the 450–1040 nm range. We found that for μ_a, the overall average R^2 was 0.996, with an average root mean squared error (RMSE) of 0.004 mm^{-1}. For μ_s', the overall average R^2 was 0.993, with an average RMSE of 0.09 mm^{-1}. Compared with other systems with R^2 of 0.94 and 0.96 for μ_a and μ_s', respectively [19], the present system demonstrates greater linearity across its operating wavelengths.

3.3. Performance evaluation of the system light penetration depth

3.3.1. Analysis of light penetration depth based on diffuse reflection values

A key advantage of SFDI technology lies in its depth-resolved imaging capability. As demonstrated in Fig. 6(a), diffuse reflectance maps acquired at 740 nm reveal distinct depth discrimination across multiple spatial frequencies. Lower f_x (0 mm^{-1}) enabled the visualization of 4-mm-diameter subject phantoms at a depth of 3 mm, while maintaining 2 mm detection sensitivity for narrower 2-mm-diameter targets. Progressive increases in frequency to 0.07 mm^{-1} reduced the effective detection depth to less than 2 mm for 4-mm phantoms, with complete signal attenuation observed beyond an f_x of 0.30 mm^{-1}. Diffuse reflectance maps of the phantom pool at multiple wavelengths (f_x= 0 mm^{-1}) are shown in Fig. 6(b), which directly reflects the influence of wavelength on light penetration ability. The lateral intensity profiles in Fig. 6(c) quantify this depth frequency relationship through PVR analysis. Shallow targets (Tubes 1 and 2) maintained a PVR > 1.53 across all frequencies, indicating robust 1 mm depth detection. Conversely, deeper phantoms (Tube 5) exhibited PVR degradation from 1.53 to 1.12 with increasing frequency, confirming reduced penetration capability. The maximum resolvable depth under multifrequency interrogation reached 3 mm. Notably, wavelength-dependent effects significantly enhanced depth performance (Fig. 6(d)). As μ_a decreased at longer wavelengths (950–1030 nm, per Fig. 5(e)), the reduced attenuation of the background phantom improved the PVR, enabling the detection of Tube 8 phantoms at a depth of 4 mm. These results collectively demonstrate that the SFDI detection depth (3–4 mm) is governed by synergistic wavelength frequency optimization.

3.3.2. Analysis of light penetration depth based on optical properties

Fig. 7(a) shows a comparison of optical properties maps of the phantom pool at different wavelengths. Since the phantom pool constructed in this study primarily differentiates the target from the background based on μ_a, the detectable depth is reflected mainly in the μ_a maps. The trend of the detectable depth is consistent with the change in diffuse reflectance at zero f_x at different wavelengths; both show an increased contrast between the target region and the background with increasing wavelength, leading to a greater detection depth. Since the μ_a of the ink solution and the μ_s' of the Intralipid-20% solution both decreased with increasing wavelength within the experimental wavelength range, deeper light penetration was achieved at higher wavelengths. The intensity profiles in Fig. 7(b) also demonstrate the same conclusion, with the maximum detectable depth being approximately 3–4 mm.

3.4. Measurement of the optical properties of fruits

3.4.1. Validation of the agreement between the SFDI- and IS-measured optical properties

A comparison of the optical properties of the fruit samples measured by the SFDI and IS systems is shown in Fig. 8. The SFDI measurements are generally in good agreement with those from the IS system. However, the wavelength resolution of the SFDI system is lower than that of the IS system because of the 10 nm interval used

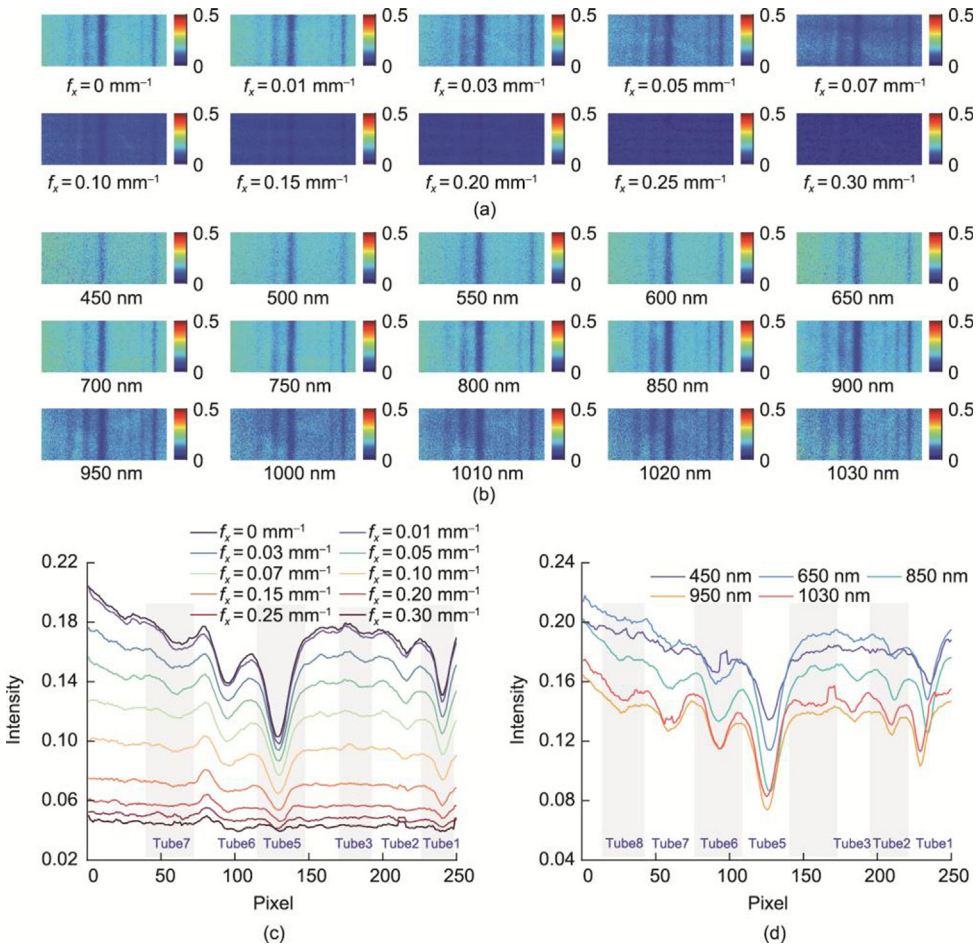

Fig. 6. Schematic of penetration depth based on diffuse reflection intensity. (a) Diffuse reflection maps of the phantom pool at different f_x (740 nm); (b) diffuse reflection maps of the phantom pool at multiple wavelengths (f_x = 0 mm^{-1}); (c) comparison of the lateral profile intensity of diffuse reflection at different f_x (740 nm); (d) comparison of the lateral profile intensity of diffuse reflection at multiple wavelengths (f_x = 0 mm^{-1}).

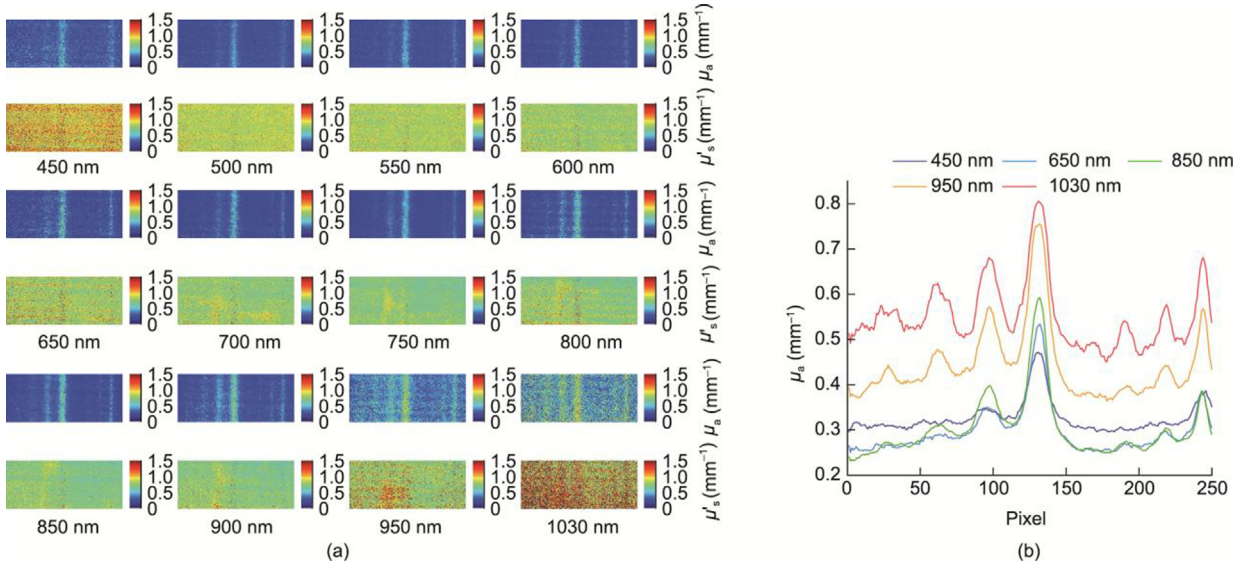

Fig. 7. (a) μ_a and μ'_s of the phantom pool at different wavelengths. (b) Comparison of the lateral profile intensity of the μ_a at multiple wavelengths.

for SFDI image acquisition, resulting in less smooth curves in the figure compared with the IS curves.

For μ_a, absorption peaks can be observed near 670 and 740 nm in peach, apple, and pear pulp, primarily because of the high chlorophyll content in the tissues. The absorption peak near 980 nm is attributed to the second overtone corresponding to –OH ions in carbohydrates [46]. The absorption of anthocyanins and carotenoids in the pulp tissue near 500 nm [47] causes the

overall μ_a to initially decrease but then increase between 450 and 1040 nm, with varying degrees of fluctuation due to absorption by chlorophyll and other components.

The μ_s' of biological tissues typically tends to decrease with increasing wavelength [48]. Reported studies on these three fruits have shown similar trends in the measured μ_s', but the measurement results vary across different systems. Some studies have reported a decreasing trend similar to that of biological tissues [43,49–51]. Other studies have reported that the μ_s' of apple pulp tissue decreases within specific wavelength ranges, such as 550–1040 nm, but the μ_s' is overestimated in the 400–550 nm range due to crosstalk from carotenoids [52]. Similar trends have also been observed in peach pulp tissue, particularly a concave trend in the μ_s' at corresponding strong absorption wavelengths such as 510, 670, 740, and 970 nm. These phenomena may be attributed to the system overestimating absorption and neglecting light loss [53]. In this study, we reported that the measured μ_s' of the fruit pulp exhibits an increasing trend before 700 nm and a decreasing trend between 700 and 1040 nm. Both the IS and SFDI systems show this trend. Crosstalk in the IS may be manifested as an underestimation of μ_s' at 980 nm due to strong water absorption. Overall, the trends in μ_s' are very similar. The average measurement errors are 0.002 mm^{-1} for μ_a and 0.02 mm^{-1} for μ_s'.

Fig. 9 shows a schematic of the optical property measurement results of a peach using the constructed SFDI system. The figure also shows that the μ_s' of the peach varies little at different wavelengths, while the μ_a near 500 and 950 nm is greater than that between 600 and 900 nm because of the absorption of chemical components. Furthermore, we also observed that μ_a and μ_s' are not uniformly distributed across the entire peach cross-section. The μ_s' near the edge region is greater than that in the central region, whereas the μ_a does not exhibit a consistent pattern at different wavelengths. We will further investigate the nonuniform distribution of optical properties in fruits under a wide FOV in the next section.

3.4.2. Heterogeneous distribution of optical properties in fruit

Based on the wide-field optical property distributions obtained from the peach, as shown in Fig. 10(a), we selected two data lines originating from the center of the fruit: one horizontal and one vertical. By extracting data along these lines, we generated optical property profiles from the fruit's skin edge to its center, as shown in Figs. 10 (b)–(e). We present the results for three wavelengths, 510, 670, and 970 nm, corresponding to absorption peaks near anthocyanins, chlorophyll, and water, respectively.

According to Figs. 10(b) and (d), absorption at 510 nm is significantly greater than that at other wavelengths. Furthermore, the μ_a at 510 nm gradually decreases from the skin to the center of the cross-section, indicating a nonuniform distribution of anthocyanins within the observed plane. The μ_a at 670 and 970 nm slightly decreases with increasing distance from the skin. The slight increase at the end of the curves might be due to the selected cross-section intersecting the pit region. The 670 nm μ_a curve suggests a gradual decrease in chlorophyll content from the skin toward the inner mesocarp. This finding aligns with the results of Rodriguez et al. [54], who analyzed the early development stages of peach fruit and reported that the chlorophyll a content in the outer mesocarp was approximately 20 times greater than that in the inner mesocarp. The 970 nm μ_a curve suggests that the water content in the exocarp of the peach fruit may be greater than that in the mesocarp and endocarp. A magnetic resonance imaging (MRI) study also found that the transverse relaxation time (T_2) value of the exocarp was greater than that of the endocarp in mature peaches, indicating a potentially higher water content or free water content in cell vacuoles in the exocarp [55]. These results demonstrate that differences in the content of absorption-related components can be characterized using wide-field absorption property maps.

The curves of μ_s' on the horizontal and vertical data lines as a function of the distance from the fruit peel surface are shown in Figs. 10(c) and (e). The data at different wavelengths overlap well, which is consistent with our μ_s' results from the previous section, indicating that there is no significant spectral dependence. However, the trends of the transverse and longitudinal curves differ. In the longitudinal direction, μ_s' initially increases but then decreases with increasing distance from the skin. In contrast, μ_s' in the horizontal direction decreases. Lohner et al. [16] reported a decrease followed by an increase in μ_s' from the skin to the core

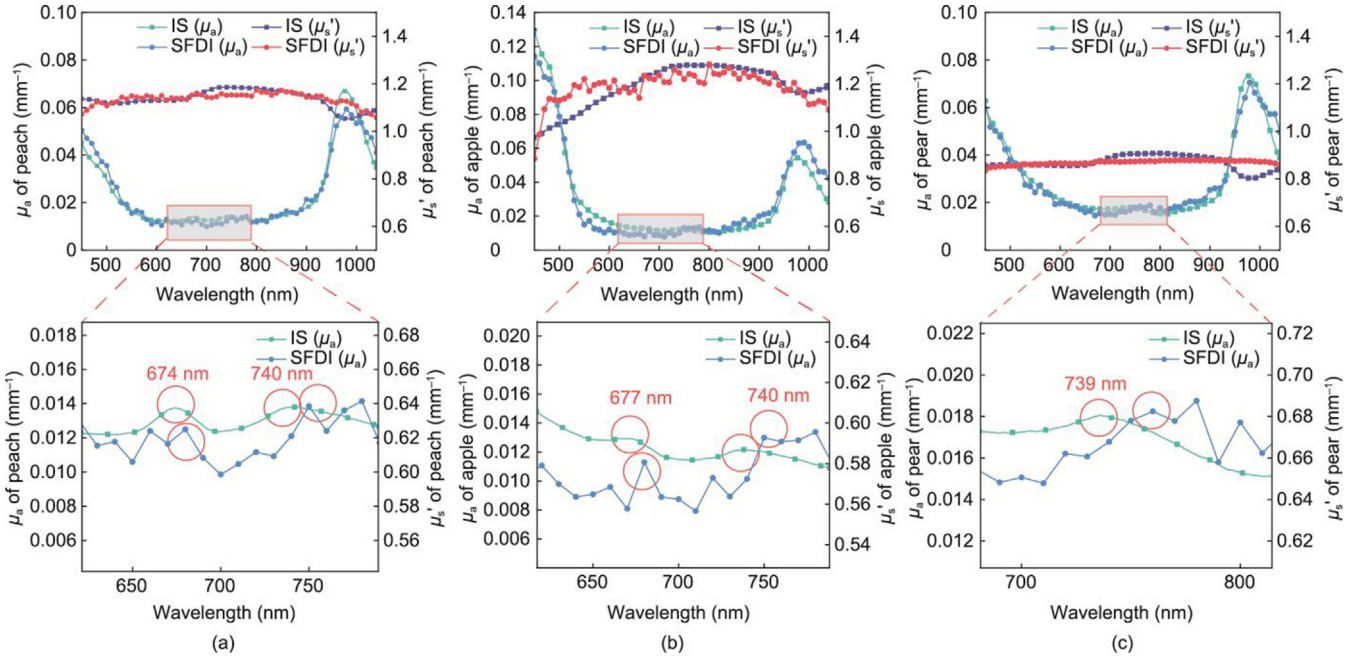

Fig. 8. Comparison of the optical properties of the fruit samples measured by the SFDI system and IS system: (a) peach, (b) apple, and (c) pear.

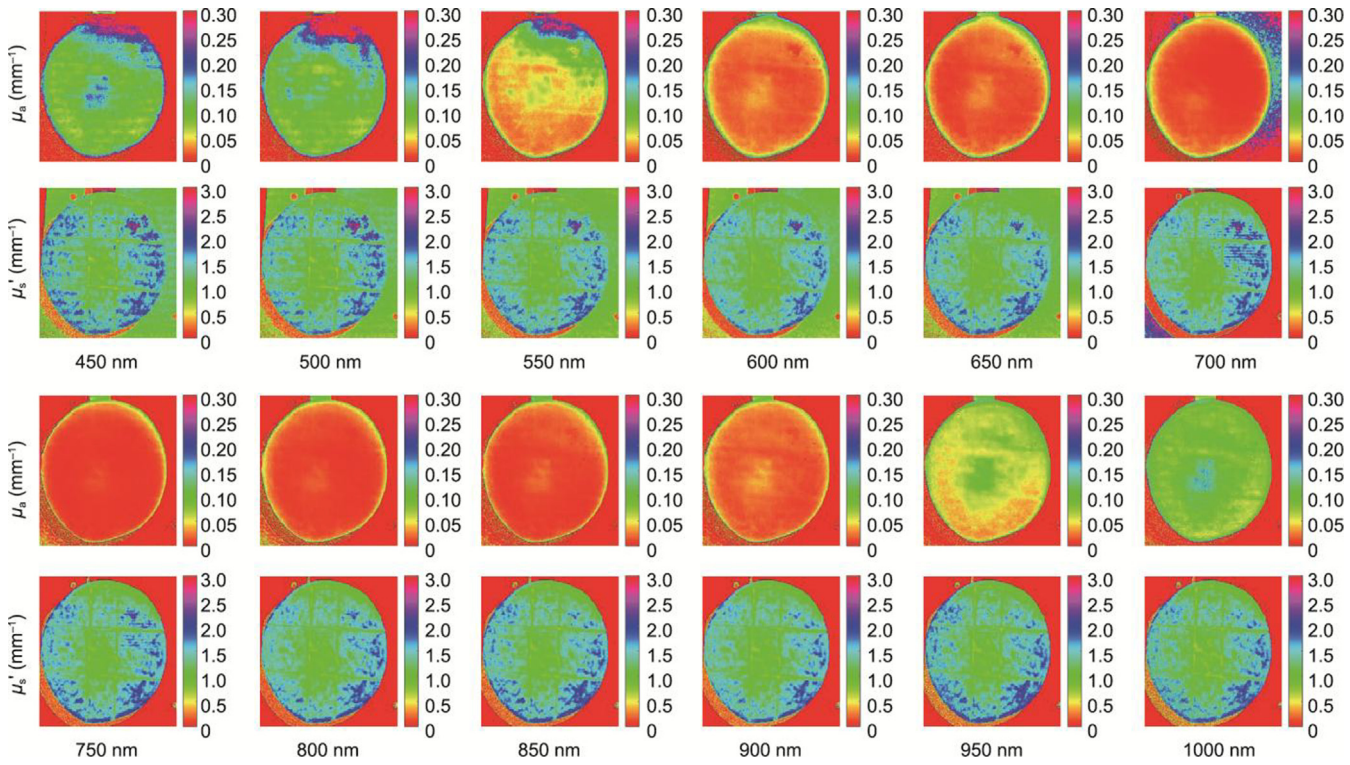

Fig. 9. Illustration of the optical property measurement results of a peach obtained with the constructed SFDI system.

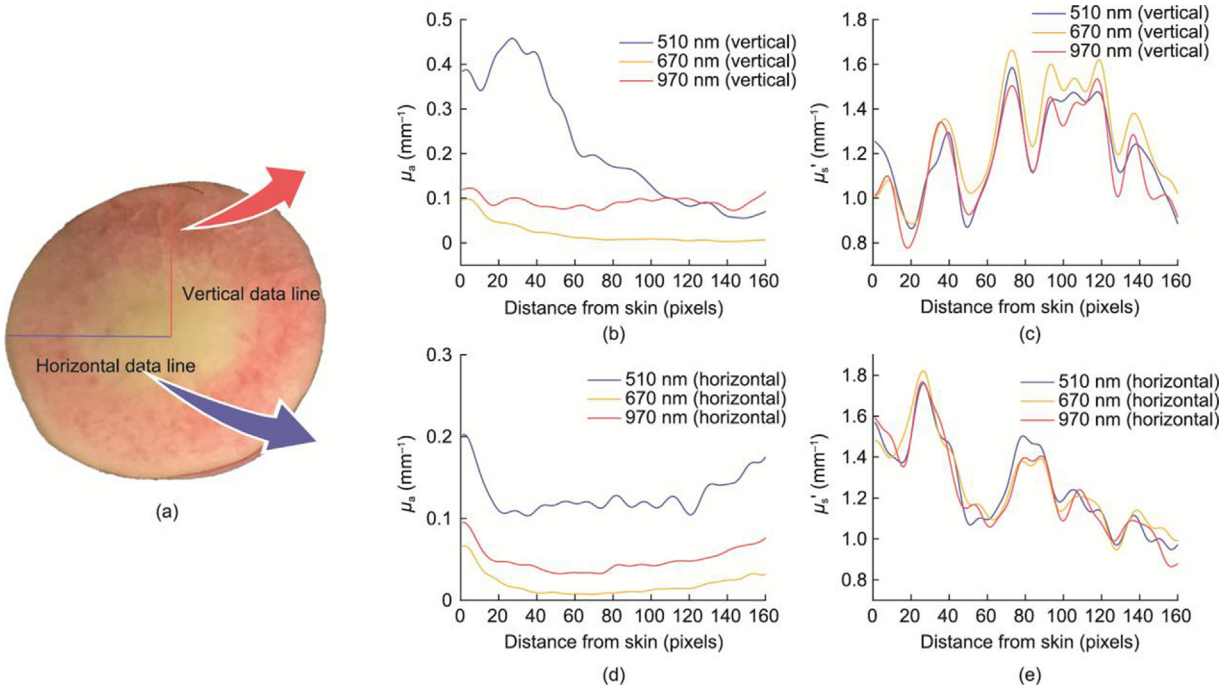

Fig. 10. (a) RGB image of the equatorial cross-section of a peach, illustrating the optical property data extraction lines (horizontal and vertical). (b) and (c) are the μ_a and μ_s' profiles, respectively, along the vertical data line. (d) and (e) are the μ_a and μ_s' profiles, respectively, along the horizontal data line.

region in apple slices. They also reported that the application of the semi-infinite model can lead to larger measurement errors near the skin. Although a higher μ_s' should be observed in the skin than in the flesh [56], the thinness of the skin and edge measurement errors along the cross-section may lead to discrepancies in the actual measurements.

Overall, variations in intercellular spaces, cell wall thickness, and the nonuniform distribution of water content or plant pigments can lead to significant changes in optical properties. The measurements indicate that the optical properties of the peaches measured under wide-field imaging exhibit significant heterogeneity. The average differences in μ_a along the vertical and horizontal

directions at all measured wavelengths are 0.18 and 0.21 mm^{-1}, respectively. The average differences in μ_s' along the vertical and horizontal directions are 1.28 and 1.96 mm^{-1}, respectively.

3.5. Peach firmness prediction results

To investigate the correlation between optical properties and peach firmness, PLSR-based quantitative models were established. Table 2 summarizes the prediction results. For all the input variables, the R_c^2 values were consistently greater than the R_p^2 values, suggesting that the models were not overfit and exhibited good reliability. Among the tested models, the μ_a-based PLSR model achieved the best predictive performance (R_p^2 = 0.786, RMSEP = 1.038 N), outperforming models based on μ_s' as well as combined parameters such as $\mu_a \times \mu_s'$ and μ_{eff}.

Previous studies have reported that combining μ_a and μ_s' can improve firmness prediction in apples, as cell wall pectin-related absorption and scattering properties jointly reflect softening behavior [57]. Other research on 'Korla' pears demonstrated that μ_{eff} in the 905–1500 nm range provided the best PLSR model for firmness (R_p^2 = 0.893) and suggested that μ_s' and μ_{eff} were more closely linked to fruit microstructural attributes than μ_a [58].

However, in our experiments, the μ_a-based model outperformed those using scattering or combined parameters. A possible explanation is the variability in fruit maturity within the sample set, where chlorophyll absorption peaks may have contributed additional information relevant to firmness prediction. SFDI-based approaches for internal fruit quality assessment remain limited. Peng et al. [59] developed firmness models for apples using optical properties at 460, 527, 630, and 710 nm and reported that μ_{eff} provided the best predictions, although the R_p^2 was modest (0.62). Similarly, He et al. [17] modeled firmness in pears at 460, 503, 527, 630, 658, and 675 nm, with the best μ_s'-based prediction yielding an R_p^2 of only 0.539. Compared with these studies, which rely on a limited number of discrete wavelengths, our results demonstrate a significantly improved predictive ability, highlighting the promising potential of SFDI for the quantitative evaluation of fruit firmness.

3.6. Comparison with other systems

To further demonstrate the superiority of our developed continuously tunable wavelength SFDI system, we compared its performance with that of related studies, as shown in Table 3 ([19,22,24,26,60]). A key advantage of our SFDI system over others is its ability to achieve a broad wavelength range (450–1040 nm) without the need for additional hardware configurations. Furthermore, compared with other methods, our system achieved the lowest μ_a measurement error (5.06%) on optical phantoms. The relative error in μ_s' was slightly greater than that in other studies, which may be attributed to minor differences between the actual composition of the Intralipid solution we used and that reported in the literature.

3.7. Advantages, limitations, and future plan

3.7.1. Advantages and limitations

Overall, our system provides unique advantages in the wavelength domain. Compared with previous multispectral or hyperspectral SFDI systems, the proposed system features a compact, customizable wavelength selection mechanism without mechanical scanning, ensuring higher imaging efficiency. Its modular configuration also offers high flexibility. Together with our automated acquisition software and a deep learning-based demodulation algorithm, the number of images required at each wavelength was reduced to one-sixth of that in conventional systems [29]. This rapid image acquisition capability lays the foundation for extending measurements to a larger number of wavelengths. SFDI plays an important role in fruit quality inspection and in studies of light transport mechanisms in biological tissues. Based on our literature review [61], we find that the spectral expansion of SFDI remains limited. For fruits such as apples, the presence of carotenoids, anthocyanins, chlorophyll, and water leads to characteristic absorption peaks at multiple wavelengths. Multispectral or hyperspectral optical properties measurements are therefore critical for predicting internal fruit quality and for structural assessments such as early bruise detection [19,62]. The optical properties measurements of the peach, apple, and pear samples revealed that the average measurement errors of the proposed system were 0.002 mm^{-1} for μ_a and 0.02 mm^{-1} for μ_s', demonstrating its high measurement accuracy. With its multiwavelength and high-precision measurement capability, the system provides an important foundation for modeling fruit quality parameters. Compared with IS systems, the proposed system enables wide-field and depth-resolved measurements, achieving simultaneous acquisition in both the spatial and spectral domains.

The current system is limited to a spectral range up to approximately 1040 nm because of the optical coating of the projection module lenses. In addition, as with other commonly used single IS systems, calibration is required before each measurement, i.e., acquiring reference whiteboard images for all working wavelengths, which is a relatively time-consuming process. Nevertheless, owing to the modular design, the system can be upgraded in future work by replacing the DMD projection module with components coated for different wavelength ranges, thereby extending the imaging window into the NIR II region. Reducing optical scattering in the shortwave infrared region can further increase the imaging depth in fruit tissues, providing a basis for internal quality assessment. Another limitation is the finite spectral resolution. To ensure sufficient light intensity at the monochromator output coupled into the fiber, we used a relatively wide slit, which reduced the system's spectral resolution.

3.7.2. Future plan

(1) Further extension of imaging wavelengths: In the NIR II window, the second overtone of the C–H stretching in carbohydrates and the combined O–H overtones give rise to an absorption peak at 1190 nm. At approximately 1450 nm, a stronger water absorption peak occurs, corresponding to the first overtone of O–H

Table 2
Peach firmness prediction results based on μ_a, μ_s', and their combinations.

Optical properties	Calibration set		Prediction set	
	R_c^2	RMSEC (N)	R_p^2	RMSEP (N)
μ_a	0.881	0.970	0.786	1.038
μ_s'	0.815	1.166	0.725	1.287
$\mu_a \times \mu_s'$	0.854	1.069	0.697	1.248
μ_{eff}	0.921	0.767	0.637	1.457

Table 3
Comparison of key parameters of the proposed SFDI system with other SFDI systems.

Light source	Wavelength selector	Spectral range (nm)	Spectral sampling interval (nm)	Measurement error		Application	References
				μ_a	μ_s'		
LED	Bandpass filters	460, 530, 632	—	11%	3%	Optical characterization of tissue-simulating intralipid phantoms and mouse brain tissue	[60]
QTH lamp	LCTF	650–950	20	—	—	Bruise detection of apples	[26]
QTH Lamp	DMD	731–863	17.5	23%	6%	Blood stain spectral monitoring	[22]
QTH lamp	—	450–740	~5.27	9.24%	6.08%	Optical properties measurement of milk	[24]
QTH lamp	Bandpass filters	550, 600, 630, 675, 710, 730	—	8.56%	5.80%	Early-stage bruise detection of fruits and vegetables	[19]
Xenon lamp	Monochromator	450–1040	10	5.06%	7.53%	Optical properties measurement of fruits	This study

DMD: digital micromirror device.

stretching. These spectral features can provide more comprehensive information for fruit quality assessment [58,63]. Since the theoretical working wavelength of the monochromator, optical fibers, and infrared camera in our system can reach 1700 nm, the imaging range could in principle be extended to 1700 nm in future work simply by replacing the projector to avoid coating-related transmission loss in the infrared region. To achieve an even broader-band SFDI system, however, a redesign of the optical path would be required to ensure stable switching among projection components operating at different wavelength ranges.

(2) Multimodal integration: Integrating multisource information will facilitate a more comprehensive characterization of fruit tissue. Recent studies have explored multimodal SFDI systems that combine hyperspectral imaging, SFDI, and fluorescence spectroscopy, where fluorescence provides access to fluorophores that are difficult to detect using reflection-based techniques [64]. In future work, we plan to integrate the existing SFDI system with other imaging or spectroscopic modalities—for instance, combining it with spectroscopic techniques to simultaneously access deeper tissue information or coupling it with multiphoton microscopy to provide microstructural details of fruit tissues. Such integration would help elucidate the relationship between optical properties and microscopic cellular structures.

(3) Further investigation of light transport: Although our phantom experiments allow estimation of penetration depth in reflectance maps, the actual light transport behavior within fruit tissues remains insufficiently understood. In future studies, we plan to combine Monte Carlo optical simulations to investigate light transport patterns in fruit tissues under different spatial frequencies and wavelengths while simultaneously developing a transmission spectroscopy scanning system to collect SR transmission data for validation. Ultimately, we aim to establish a framework that decouples the interactions among optical properties, light transport modes, and key quality attributes of fruits, thereby providing a solid foundation for optical-based fruit quality assessment technologies.

4. Conclusions

In this study, we successfully developed and characterized a continuously tunable wavelength (450–1040 nm) SFDI system for the nondestructive assessment of fruit quality. The system integrates a high-performance monochromator, a DMD-based pattern projection module, and a sensitive shortwave infrared camera, enabling high-resolution optical properties measurements across a broad spectral range. Comprehensive system characterization revealed a spatial resolution of 3.17 lp·mm^{-1} and good wavelength accuracy, with an average peak wavelength deviation of 5.1 nm. Uniformity correction significantly improved image homogeneity, and the system's linearity was validated using solid phantoms, achieving high fitting accuracy (R_2 > 0.99) for both μ_a and μ_s'. Light penetration depth analysis using a constructed phantom pool revealed that, for background phantoms simulating fruit peel optical properties, light penetration depths of 3–4 mm could be reached at specific wavelength and f_x combinations. Furthermore, the system's accuracy in measuring fruit optical properties was confirmed by comparing the SFDI results with those obtained from a calibrated IS system, which demonstrated good agreement for the peach, apple, and pear samples. Wide-field imaging revealed significant heterogeneity in the optical properties of peaches, highlighting the potential of SFDI for mapping compositional variations within fruit. Compared with existing SFDI systems, our design offers a broader continuously tunable wavelength range and competitive measurement accuracy. This versatile SFDI system provides a powerful tool for nondestructive fruit grading and quality evaluation and, potentially, for obtaining deeper insights into fruit physiology and composition. Future work will focus on expanding the system's spectral range into the NIR II region and developing quantitative models to predict fruit internal quality parameters based on SFDI-derived optical properties.

CRediT authorship contribution statement

Yuan Gao: Writing – original draft, Software, Methodology, Formal analysis, Data curation. **Zhizhong Sun:** Validation, Software, Methodology, Data curation. **Xuan Luo:** Conceptualization, Data curation, Writing – review & editing. **Dong Hu:** Writing – review & editing, Methodology, Conceptualization. **Benhui Dai:** Writing – review & editing, Formal analysis, Data curation. **Yingjie Zheng:** Writing – review & editing, Data curation. **Yibin Ying:** Writing – review & editing, Supervision, Resources, Project administration, Conceptualization. **Lijuan Xie:** Writing – review & editing, Validation, Supervision, Resources, Project administration, Funding acquisition, Formal analysis, Conceptualization.

Declaration of competing interest

The authors declare that they have no known competing financial interests or personal relationships that could have appeared to influence the work reported in this paper.

Acknowledgments

This work was supported by the National Key Research and Development Program of China (2023YFD2201300) and the integrated pilot project of agricultural machinery research and development, manufacturing, promotion, and application of the Zhejiang Provincial Department of Agriculture and Rural Affairs. The authors would also like to thank the helpful comments and suggestions provided by all the authors cited in this article and the anonymous reviewers.

Appendix A. Supplementary data

Supplementary data to this article can be found online at https://doi.org/10.1016/j.eng.2026.01.029.

References

[1] Akter T, Bhattacharya T, Kim JH, Kim MS, Baek I, Chan DE, et al. A comprehensive review of external quality measurements of fruits and vegetables using nondestructive sensing technologies. J Agric Food Res 2024;15:101068.
[2] He L, Sun Y, Chen L, Feng Q, Li Y, Lin J, et al. Advance on agricultural robot hand–eye coordination for agronomic task: a review. Engineering 2025;51:263–79.
[3] Lu R, Van Beers R, Saeys W, Li C, Cen H. Measurement of optical properties of fruits and vegetables: a review. Postharvest Biol Technol 2020;159:111003.
[4] Zhang X, Yang J. Advanced chemometrics toward robust spectral analysis for fruit quality evaluation. Trends Food Sci Technol 2024;150:104612.
[5] Hu D, Jia T, Sun X, Zhou T, Huang Y, Sun Z, et al. Applications of optical property measurement for quality evaluation of agri-food products: a review. Crit Rev Food Sci Nutr 2024;64(33):12599–619.
[6] Cuccia DJ, Bevilacqua F, Durkin AJ, Tromberg BJ. Modulated imaging: quantitative analysis and tomography of turbid media in the spatial-frequency domain. Opt Lett 2005;30(11):1354–6.
[7] Anderson ER, Cuccia DJ, Durkin AJ. Detection of bruises on golden delicious apples using spatial-frequency-domain imaging. In: Proceedings Volume 6430, Advanced Biomedical and Clinical Diagnostic Systems V; 2007 Jan 20–25; San Jose, CA, USA. Bellingham: SPIE; 2007. p. 308–18.
[8] Hu D, Lu R, Ying Y, Fu X. A stepwise method for estimating optical properties of two-layer turbid media from spatial-frequency domain reflectance. Opt Express 2019;27(2):1124–41.
[9] Hu D, Lu R, Ying Y. Finite element simulation of light transfer in turbid media under structured illumination. Appl Opt 2017;56(21):6035–42.
[10] Hu D, Fu X, He X, Ying Y. Noncontact and wide-field characterization of the absorption and scattering properties of apple fruit using spatial-frequency domain imaging. Sci Rep 2016;6(1):37920.
[11] Lu Y, Li R, Lu R. Detection of fresh bruises in apples by structured-illumination reflectance imaging. In: Kim MS, Chao K, Chin BA, editors. Proceedings Volume 9864, Sensing for Agriculture and Food Quality and Safety VIII; 2016 Apr 17–21; Baltimore, MD, USA. Bellingham: SPIE; 2016. p. 986406.
[12] Lu Y, Lu R. Structured-illumination reflectance imaging for the detection of defects in fruit: analysis of resolution, contrast and depth-resolving features. Biosyst Eng 2019;180:1–15.
[13] Dögnitz N, Wagnières G. Determination of tissue optical properties by steady-state spatial frequency-domain reflectometry. Lasers Med Sci 1998;13:55–65.
[14] Lu Y, Li R, Lu R. Fast demodulation of pattern images by spiral phase transform in structured-illumination reflectance imaging for detection of bruises in apples. Comput Electron Agric 2016;127:652–8.
[15] Lu Y, Li R, Lu R. Structured-illumination reflectance imaging (SIRI) for enhanced detection of fresh bruises in apples. Postharvest Biol Technol 2016;117:89–93.
[16] Lohner SA, Biegert K, Nothelfer S, Hohmann A, McCormick R, Kienle A. Determining the optical properties of apple tissue and their dependence on physiological and morphological characteristics during maturation. Part 1: spatial frequency domain imaging. Postharvest Biol Technol 2021;181:111647.
[17] He X, Yang X, Fu X, Jiang X, Rao X. Assessing soluble solid content and texture of pear during shelf-life period by single snapshot spatial frequency domain imaging. Biosyst Eng 2021;212:252–63.
[18] Yang Y, Fu X, Zhou Y. Hyperspectral spatial frequency domain imaging technique for soluble solids content and firmness assessment of pears. Horticulturae 2024;10(8):853.
[19] Sun Z, Hu D, Zhou T, Sun X, Xie L, Ying Y. Development of a multispectral spatial-frequency domain imaging system for property and quality assessment of fruits and vegetables. Comput Electron Agric 2023;214:108251.
[20] Applegate M, Karrobi K, Angelo J, Austin W, Tabassum S, Aguénounon E, et al. OpenSFDI: an open-source guide for constructing a spatial frequency domain imaging system. J Biomed Opt 2020;25(1):1–13.
[21] Torabzadeh M, Stockton P, Kennedy G, Saager R, Durkin AJ, Bartels R, et al. Hyperspectral imaging in the spatial frequency domain with a supercontinuum source. J Biomed Opt 2019;24(7):1–9.
[22] Applegate MB, Spink SS, Roblyer D. Dual-DMD hyperspectral spatial frequency domain imaging (SFDI) using dispersed broadband illumination with a demonstration of blood stain spectral monitoring. Biomed Opt Express 2021;12(1):676–88.
[23] Singh-Moon RP, Roblyer DM, Bigio IJ, Joshi S. Spatial mapping of drug delivery to brain tissue using hyperspectral spatial frequency-domain imaging. J Biomed Opt 2014;19(9):096003.
[24] Luo Y, Dai L, Jiang X, Fu X. Measurement of absorption and scattering properties of milk using a hyperspectral spatial frequency domain imaging system. J Food Meas Charact 2022;16(1):753–61.
[25] Weber JR, Cuccia DJ, Johnson WR, Bearman GH, Durkin AJ, Hsu M, et al. Multispectral imaging of tissue absorption and scattering using spatial frequency domain imaging and a computed-tomography imaging spectrometer. J Biomed Opt 2011;16(1):011015.
[26] Lu Y, Lu R. Development of a multispectral structured illumination reflectance imaging (SIRI) system and its application to bruise detection of apples. Trans ASABE 2017;60(4):1379–89.
[27] Zhou T, Hu D, Qiu D, Yu S, Huang Y, Sun Z, et al. Analysis of light penetration depth in apple tissues by depth-resolved spatial-frequency domain imaging. Foods 2023;12(9):1783.
[28] Cuccia DJ, Bevilacqua F, Durkin AJ, Ayers FR, Tromberg BJ. Quantitation and mapping of tissue optical properties using modulated imaging. J Biomed Opt 2009;14(2):024012.
[29] Gao Y, Sun Z, Hu D, Xie L, Ying Y. GMOPNet: A GAN-MLP two-stage network for optical properties measurement of kiwifruit and peaches with spatial frequency domain imaging. Food Chem 2025;465(Pt 1):141944.
[30] Gebhart SC, Thompson RC, Mahadevan-Jansen A. Liquid-crystal tunable filter spectral imaging for brain tumor demarcation. Appl Opt 2007;46(10):1896–910.
[31] Wang W, Li C, Tollner EW, Rains GC, Gitaitis RD. A liquid crystal tunable filter based shortwave infrared spectral imaging system: calibration and characterization. Comput Electron Agric 2012;80:135–44.
[32] Jia J, Wang Y, Zheng X, Yuan L, Li C, Cen Y, et al. Design, performance, and applications of AMMIS: a novel airborne multimodular imaging spectrometer for high-resolution earth observations. Engineering 2025;47:38–56.
[33] Luo Y, Jiang X, Fu X. Spatial frequency domain imaging system calibration, correction and application for pear surface damage detection. Foods 2021;10(9):2151.
[34] Bouchard JP, Veilleux I, Jedidi R, Noiseux I, Fortin M, Mermut O. Reference optical phantoms for diffuse optical spectroscopy. Part 1—error analysis of a time resolved transmittance characterization method. Opt Express 2010;18(11):11495–507.
[35] Tian S, Tian H, Yang Q, Xu H. Internal quality assessment of kiwifruit by bulk optical properties and online transmission spectra. Food Control 2022;141:109191.
[36] Prahl SA, van Gemert MJC, Welch AJ. Determining the optical properties of turbid media by using the adding-doubling method. Appl Opt 1993;32(4):559–68.
[37] Aernouts B, Zamora-Rojas E, Van Beers R, Watté R, Wang L, Tsuta M, et al. Supercontinuum laser based optical characterization of Intralipid® phantoms in the 500–2250 nm range. Opt Express 2013;21(26):32450–67.
[38] Deng R, He Y, Qin Y, Chen Q, Chen L. Pure water absorption coefficient measurement after eliminating the impact of suspended substance in spectrum from 400 nm to 900 nm. Nat Remote Sens Bull 2012;16(1):174–91. Chinese.
[39] Deng R, He Y, Qin Y, Chen Q, Chen L. Measuring pure water absorption coefficient in the near-infrared spectrum (900–2500 nm). Nat Remote Sens Bull 2012;16(1):192–206. Chinese.
[40] Goldfain AM, Lemaillet P, Allen DW, Briggman KA, Hwang J. Polydimethylsiloxane tissue-mimicking phantoms with tunable optical properties. J Biomed Opt 2021;27(7):074706.
[41] Hwang J, Kim HJ, Lemaillet P, Wabnitz H, Grosenick D, Yang L, et al. Polydimethylsiloxane tissue-mimicking phantoms for quantitative optical medical imaging standards. In: Proceedings Volume 10056, Design and Quality for Biomedical Technologies X Design and Quality for Biomedical Technologies X; 2017 Jan 28–Feb 2; San Francisco, CA, USA. Bellingham: SPIE; 2017. p. 15–20.
[42] Zhao Y, Pilvar A, Tank A, Peterson H, Jiang J, Aster JC, et al. Shortwave-infrared meso-patterned imaging enables label-free mapping of tissue water and lipid content. Nat Commun 2020;11(1):5355.
[43] Van Beers R, Aernouts B, Watté R, Schenk A, Nicolaï B, Saeys W. Effect of maturation on the bulk optical properties of apple skin and cortex in the 500–1850 nm wavelength range. J Food Eng 2017;214:79–89.
[44] Sheng R, Cheng W, Li H, Ali S, Akomeah Agyekum A, Chen Q. Model development for soluble solids and lycopene contents of cherry tomato at different temperatures using near-infrared spectroscopy. Postharvest Biol Technol 2019;156:110952.
[45] Wold S, Sjöström M, Eriksson L. PLS-regression: a basic tool of chemometrics. Chemom Intell Lab Syst 2001;58(2):109–30.
[46] Magwaza LS, Landahl S, Cronje PJR, Nieuwoudt HH, Mouazen AM, Nicolaï BM, et al. The use of Vis/NIRS and chemometric analysis to predict fruit defects and postharvest behaviour of 'Nules Clementine' mandarin fruit. Food Chem 2014;163:267–74.
[47] Tian K, Zhu W, Wang M, Chen T, Li F, Xie J, et al. Qualitative and quantitative assessment of apple quality using bulk optical properties in combination with machine learning and chemometrics techniques. Lebensm Wiss Technol 2024;211:116894.
[48] Bashkatov A, Genina E, Kochubey V, Tuchin V. Optical properties of the subcutaneous adipose tissue in the spectral range 400–2500 nm. Opt Spectrosc 2005;99(5):836–42.
[49] Cen H, Lu R, Mendoza FA, Ariana DP. Assessing multiple quality attributes of peaches using optical absorption and scattering properties. Trans ASABE 2012;55:647–57.
[50] Hu D, Fu X, Ying Y. Characterizing pear tissue with optical absorption and scattering properties using spatially-resolved diffuse reflectance. J Food Meas Charact 2017;11(2):930–6.
[51] Sun Y, Lu R, Pan L, Wang X, Tu K. Assessment of the optical properties of peaches with fungal infection using spatially-resolved diffuse reflectance technique and their relationships with tissue structural and biochemical properties. Food Chem 2020;321:126704.

[52] Wei K, Ma C, Sun K, Liu Q, Zhao N, Sun Y, et al. Relationship between optical properties and soluble sugar contents of apple flesh during storage. Postharvest Biol Technol 2020;159:111021.
[53] Ma C, Feng L, Pan L, Wei K, Liu Q, Tu K, et al. Relationships between optical properties of peach flesh with firmness and tissue structure during storage. Postharvest Biol Technol 2020;163:111134.
[54] Rodriguez CE, Bustamante CA, Budde CO, Müller GL, Drincovich MF, Lara MV. Peach fruit development: a comparative proteomic study between endocarp and mesocarp at very early stages underpins the main differential biochemical processes between these tissues. Front Plant Sci 2019;10:715.
[55] Musse M, Bidault K, Quellec S, Brunel B, Collewet G, Cambert M, et al. Spatial and temporal evolution of quantitative magnetic resonance imaging parameters of peach and apple fruit-relationship with biophysical and metabolic traits. Plant J 2021;105(1):62–78.
[56] Ding C, Shi S, Chen J, Wei W, Tan Z. Analysis of light transport features in stone fruits using Monte Carlo simulation. PLoS One 2015;10(10):e0140582.
[57] Wang Z, Zuo C, Wang M, Song S, Hu Y, Song J, et al. Optical properties related to cell wall pectin contribute to determine the firmness and microstructural changes during apple softening. Postharvest Biol Technol 2024;218:113150.
[58] Fang L, Jiang M, Lan W, You S, Ding F, Tu K, et al. Assessing sugar composition and tissue structure indices of 'Korla' pear cortex using bulk optical properties in the 500–1500 nm. Postharvest Biol Technol 2023;206:112571.
[59] Peng H, Zhang C, Sun Z, Sun T, Hu D, Yang Z, et al. Optical property mapping of apples and the relationship with quality properties. Front Plant Sci 2022;13:873065.
[60] Lin AJ, Ponticorvo A, Konecky SD, Cui H, Rice TB, Choi B, et al. Visible spatial frequency domain imaging with a digital light microprojector. J Biomed Opt 2013;18(9):096007.
[61] Gao Y, Sun Z, Xie L, Ying Y. Spatial frequency domain imaging for fruit quality assessment: a comprehensive review. Trends Food Sci Technol 2025;162:105110.
[62] Tian X, Li J, Wang Q, Fan S, Huang W. A bi-layer model for nondestructive prediction of soluble solids content in apple based on reflectance spectra and peel pigments. Food Chem 2018;239:1055–63.
[63] Yu S, Liu D, Li D, Hao H, Yang M, Chen G. Exploring the effects of impact damage on optical properties of 'Korla' pears and Monte Carlo simulation of light propagation in pear tissue. Postharvest Biol Technol 2026;231:113870.
[64] Urban BE, Subhash HM. Multimodal hyperspectral fluorescence and spatial frequency domain imaging for tissue health diagnostics of the oral cavity. Biomed Opt Express 2021;12(11):6954–68.